The response of the Subtropical Front to changes in the Southern Hemisphere Westerly Winds - Evidence from models and observations.

Erik Behrens[1] and Helen Bostock[2]

[1]NIWA
[2]University of Queensland

November 26, 2022

Abstract

The location of the Subtropical Front (STF), the boundary between Subtropical and Subantarctic Water in the Southern Ocean is proposed to be controlled by the strength and location of the Southern Hemisphere westerly winds. We use a hydrodynamic hindcast model and recent observations to test if changes in the westerly winds can cause meridional shifts in the STF over interannual to decadal time scales by modulating local Ekman transport. We find that increased, or northward, shifted westerly winds lead to an enhanced northward Ekman transport over large parts of the Southern Ocean, resulting in a northward shift in the STF. Conversely for weaker or southward shifted westerly winds. Regions with strong eddy variability, such as western boundary current systems of the Agulhas and East Australian Current behave differently, as the Sverdrup balance causes an opposite shift. In these regions an increase in westerly winds lead to a southward shift in the STF. A southward shift of STF has been observed between 2004-2019. However, the shift is smaller than the latitudinal shifts in the location of the zero wind stress curl and maximum westerly winds (-0.4° latitude/decade). This discrepancy is due to positive Ekman trends resulting from the intensification of the westerly winds, which oppose the southward migration. Changes in the Ekman transport and the overall southward shift of the STF have also resulted in an observed positive trend in chlorophyll-a concentrations south of the STF, which could have ramifications for the biological pump and carbon uptake in the Southern Ocean.

The response of the Subtropical Front to changes in the Southern Hemisphere Westerly Winds – Evidence from models and observations.

Erik Behrens[1], Helen Bostock[2]

[1] National Institute of Water and Atmospheric Research, Wellington, New Zealand

[2] The University of Queensland, Brisbane, Australia

Corresponding author: Erik Behrens, erik.behrens@niwa.co.nz

Key points:

- Stronger (Weaker) westerly winds shift the location of the Subtropical Front northward (southward), except in regions of strong currents.
- The observed shift of the Subtropical Front (2004-2019) is smaller than the shift in the westerly winds, due to increased Ekman transport.
- Satellites show that southward shifts of the STF trigger a positive (negative) chlorophyll-a response south (north) of the front.

Abstract:

The location of the Subtropical Front (STF), the boundary between Subtropical and Subantarctic Water in the Southern Ocean is proposed to be controlled by the strength and location of the Southern Hemisphere westerly winds. We use a hydrodynamic hindcast model and recent observations to test if changes in the westerly winds can cause meridional shifts in the STF over interannual to decadal time scales by modulating local Ekman transport. We find that increased, or northward, shifted westerly winds lead to an enhanced northward Ekman transport over large parts of the Southern Ocean, resulting in a northward shift in the STF. Conversely for weaker or southward shifted westerly winds. Regions with strong eddy variability, such as western boundary current systems of the Agulhas and East Australian Current behave differently, as the Sverdrup balance causes an opposite shift. In these regions an increase in westerly winds lead to a southward shift in the STF. A southward shift of STF has been observed between 2004-2019. However, the shift is smaller than the latitudinal shifts in the location of the zero wind stress curl and maximum westerly winds (-0.4° latitude/decade). This discrepancy is due to positive Ekman trends resulting from the intensification of the westerly winds, which oppose the southward migration. Changes in the Ekman transport and the overall southward shift of the STF have also resulted in an observed positive trend in chlorophyll-a concentrations south of the STF, which could have ramifications for the biological pump and carbon uptake in the Southern Ocean.

Plain English Abstract:

The Subtropical Front (STF) is an important water mass barrier, between warm, salty and nutrient-depleted Subtropical Waters of the subtropical gyre to its north, and cold, fresh, but nutrient-rich Subantarctic Waters of the Southern Ocean to its south. The position of the STF is thought to be controlled by the westerly winds. In this study we investigate if the STF shifts with changes in these westerly winds. Our model experiments show that over large parts of the Southern Ocean, the changes in the location of the STF follow changes in the westerly winds, except in regions of strong oceanic currents. The observations show that between 2004-2019 a small southward trend of the STF has been detected over most parts of the Southern Ocean as a consequence of southward shift of the westerly winds due to positive Southern Annular Mode (SAM). However, the shift in the STF has not been as large as the shift in the winds, as it has been opposed by the strengthening of the westerly winds. The recent southward shift in the STF has led to an increase in plankton growth south of the STF due to increased mixing of the Subtropical and Subantarctic Waters.

1. Introduction

The Subtropical Front (STF) marks the water mass boundary between warm, salty but nutrient-depleted Subtropical Water in the subtropical gyre to its north, and cold, fresh, and nutrient-rich Subantarctic Waters in the Southern Ocean to its south (Belkin 2021; Belkin and Gordon 1996; Chapman et al. 2020; Deacon 1982; Orsi et al. 1995; Sokolov and Rintoul 2009). As such the STF is often used as the northern boundary of the Southern Ocean. Due the mixing of these two water masses the STF is a hotspot for primary production seen by elevated levels of chlorophyll-a (Chiswell et al. 2013; Pinkerton et al. 2005; Sullivan et al. 1993; Weeks and Shillington 1994), and therefore also important for carbon sequestration and fisheries.

The location of the STF is proposed to be controlled by the strength and location of the Southern Hemisphere westerly winds. However, the exact position of the STF is still not fully understood, since its location does not align with the theory that it should co-locate with the line of zero wind stress curl (De Boer et al. 2013; Tilburg et al. 2002). This knowledge gap has motivated a range of research and has led to an alternative definition of the Subtropical Front, the so called Dynamical Subtropical front, which links the STF to ocean dynamics rather than water mass properties (De Boer et al. 2013; Graham et al. 2012). Furthermore, recent research suggests that the STF will show a poleward shift as a consequence of expanding subtropical gyres due to positive Southern Annual Mode (SAM) trends shifting the southern hemisphere westerly winds south over multi-decadal timescales (Yang et al. 2020). However, equatorward shifts of the STF have also been reported, challenging the potential drivers of shorter, sub-decadal shifts (Yang et al. 2020).

In this paper we investigate the drivers of STF variability on interannual to decadal timescales using a combination of Argo, satellite, and hindcast datasets. Here we define the STF by the 11°-isotherm at 100m depth following Orsi et al. (1995). In particular we test if changes in STF location can be attributed to local changes in the Ekman transport, as a consequence of changes in the westerly winds (meridional shift, or changes in the strength of the winds, Figure 1).

In theory an increase in surface (zonal) winds would result in a stronger local Ekman transport (Figure 1b), which carries more cold Subantarctic Waters northward and would trigger a northward shift of the STF. The negative sea surface temperature (SST) anomalies would cause a positive heat flux anomaly (into the ocean) trying to compensate for the advection of cold water northward. Associated changes in the wind stress curl increase the Ekman pumping north of the STF and results in steeper isotherms, but may not necessarily generate a shift in the STF at 100m depth. Furthermore, these negative SST anomalies would lead to negative chlorophyll-a (Chl-a) anomalies in Subantarctic Waters (temperature response) and an increase in Subtropical Waters (nutrient response), relative to the mean location of the STF. This concept follows previous work in the Southern Ocean (Lovenduski 2005), but has been applied to the STF in this paper.

In the case of southward shifting winds (Figure 1c) local Ekman transport declines, which initiates a southward shift of the STF. Consequently, that leads to negative heat flux anomalies (out of the ocean) and an increase in Chl-a concentration to the south of the STF and a decline to its north. However, a reduction in Ekman pumping north of the STF shoals the isotherms, however, again it may not impact the location of the STF at 100m water depth.

In this paper we use hydrodynamic hindcast and idealized simulations with individual changes to the wind forcing using the NZ20 model (Behrens et al., 2021) in combination with in-situ and remote sensing observation data from 2004-2019 to test these conceptual models (Figure 1).

The paper is organised as follows: Section 2 introduces the data sources and methods. Section 3.1 summaries the results from sensitivity simulations where surface winds have been deliberately altered. Section 3.2 highlights where Ekman transports can be used to explain interannual variability of the STF in the Southern Ocean between 2004-2019 and section 3.3 provide insights into long-term trends. Section 4 provides a conclusion.

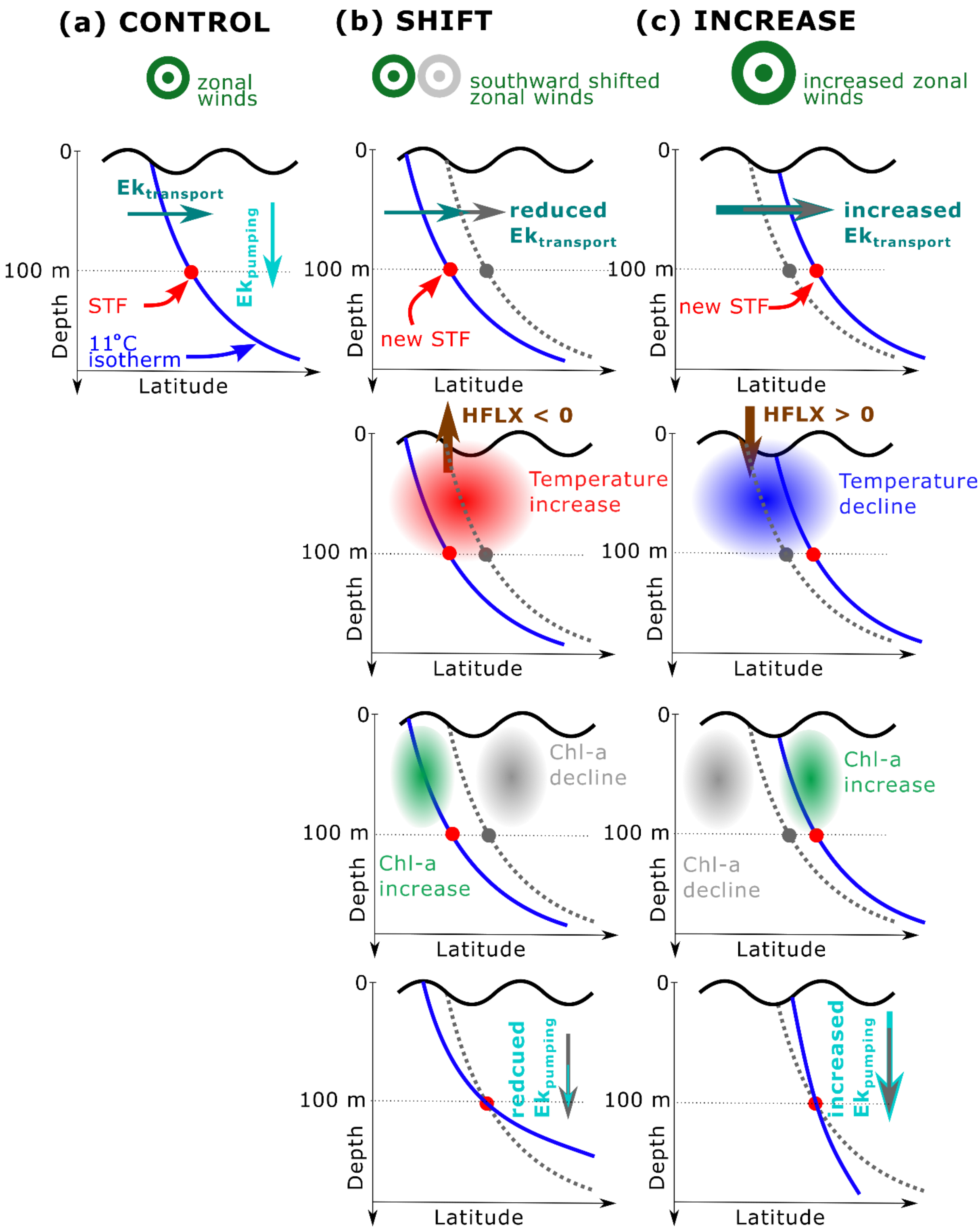

Figure 1: This Schematic shows how changes in surface winds would alter the location of the STF. (a) for the CONTROL, (b) for a southward shift of the westerly winds and (c) for an increase in westerly winds in relation to CONTROL. The blue lines mark the 11°-isotherm and the red dots showing the location of the STF at 100 m depth (as defined by Orsi et al. (1995)). In b) and c) the grey dotted lines, grey dots, and grey circles are the 11° C isotherm, STF location and winds from the CONTROL case. In (b) a southward shift of the winds leads to negative Ekman transport anomalies, and a southward shift of the STF accompanied by positive temperature anomalies. These temperature anomalies trigger positive heat flux anomalies (HFLX, from the ocean to the atmosphere) and cause a decline of Chl-a

north of the STF$_{CONTROL}$ and an increase to its south. However, reduced Ekman pumping shoals the isotherms, but may not impact the location of the STF. (c) An increase in the strength of the westerly winds leads to positive Ekman transport anomalies, and a southward shift of the STF accompanied by negative temperature anomalies and negative heat flux anomalies (from the atmosphere into the ocean). The negative SST anomalies results in negative Chl-a anomalies south of the STF$_{CONTROL}$ and positive anomalies to the north. An increase in Ekman pumping results in a steepening of the isotherms, but may not shift the STF.

2. Methods

2.1 Model simulation

This study uses data from a high-resolution (1/20°) nested ocean - sea-ice hindcast (Behrens et al. 2021). Ocean physics are simulated by NEMO 3.6 (Madec et al. 2017), while CICE version 5.2.1 (Hunke and Lipscomb 2010) has been used for sea-ice. The base for the nested model is a global eddy permitting configuration, with a nominal resolution of ¼° degree, which is known as GO6, and details of this configuration for this global setup can be found in Storkey et al. (2018). The nested region spans the ocean around New Zealand from 142.8°E to 152°W and 59°S to 22°S with a grid spacing of about 4km to fully resolve mesoscale processes (and to partially resolve sub-mesoscale dynamics). This nested model setup has been used in a related study to investigate, past variability of the STF around New Zealand (Behrens et al. 2021) and demonstrated a better performance than the global configuration without a nested region. The nesting has been facilitated by a two-way nesting scheme based on AGRIF (Debreu et al. 2008). The vertical dimension is discretized by 75-vertical z-levels, with a 1 m thick surface layer which increases to about 200 m in the deep ocean. The model uses a non-linear free surface and a partial cell approach to improve bottom flows (Barnier et al. 2006). This model simulates boundary current transports (supplementary material, Table 1) and the STF (Belkin 2021) in good agreement to observations.

In this nested setup a 62-year long model hindcast, from 1958 to 2019 has been conducted, using JRA55-DO v1.5 (Tsujino et al. 2018) atmospheric boundary conditions, hereafter CONTROL. The simulation has been started from rest with temperature and salinity fields based on the EN4 climatology (Good et al. 2013). A coastal runoff climatology has been applied, and sea surface salinity has been restored to the EN4 climatology with time scales of 30 days for the 1 m thick surface layer. In addition to the CONTROL, two sensitivity simulations have been conducted where changes to the surface winds, between 70°S to 25°S, have been applied. These simulations cover the period from 2000-2019 to test how changes in the surface winds impact the location of the STF. It is assumed that a period of 20 years is sufficient to detect a robust response in these sensitivity simulations in comparison to CONTROL.

In the first simulation the winds (zonal and meridional) are shifted south by 1-degree latitude per decade, hereafter SHIFT. Applying the anomalies to zonal and meridional winds, reduces the distortion of storms, which can otherwise result in artificial wind-stress curl anomalies (Frankcombe et al. 2013). In the second simulation an increase in zonal and meridional winds, hereafter INCREASE, of 1% per year has been applied, which reflects an increase of wind speeds by 20% at the end of 2019. Applying trends instead of step changes to winds, as done in previous studies (Frankcombe et al. 2013; Spence et al. 2010; Spence et al. 2014), was motivated to avoid initial shocks and to reduce the likelihood of spurious deep convection in the Southern Ocean (Behrens et al. 2016), which could also influence the STF response to these wind perturbations. The JRA55-DO v1.5 winds show over the period 2000-2019 in CONTROL an increasing trend in zonal winds between 0 to 0.6% per year, which varies by latitude (supplementary material, Figure S1). Over this period the location of the maximum of the zonal winds also shows a southward trend of 0.4 degrees latitude per decade. These JRA55-DO values are in-line with previous estimates (see Swart and Fyfe 2012). The imposed trends in the experiments SHIFT and INCREASE are larger than the observed trends between 2000 and 2019 and intended to simulate the general response to shifted or increased winds. However, there are some possible issues with forced models as the unavoidable thermal restoring (due to unchanged air temperatures) might limit the STF response to artificial wind changes.

2.2 Additional data sources and metrics

The Roemmich-Gilson Argo climatology (Roemmich and Gilson 2009), hereafter referred to as Argo, has been used for the comparison to model temperatures and model STF location. Furthermore, Chl-a from MODIS satellite (Sathyendranath et al. 2019) mission has been used to link Chl-a anomalies to meridional shifts in the location of the STF. The monthly mean MODIS satellite data was linearly interpolated onto a regular 1°×1° grid to allow for a direct comparison to the Argo results, which are also provided on a regular 1°×1° grid.

We apply the Orsi et al. (1995) definition to locate the STF, which uses the 11°C isotherm at 100m depth. By using temperatures at 100m depth to define the STF instead of using SSTs the seasonal variability is reduced (Orsi et al. 1995). Furthermore, temperature anomalies over the top 100m have been calculated to link them to Ekman transports and to meridional shifts of the STF. Using the top 100m averaged temperature was motivated by Ekman depths of about 75m - 100m at this latitude (Lenn and Chereskin 2009; Wang and Huang 2004), and the STF defined as the 11°C isotherm at 100m. This choice also reduces the impact of the SST 'restoring' of ocean-only models. All data sources (model and observational data) are available as monthly means, but were annually averaged to investigate interannual variability between years.

For the two wind perturbation sensitivity simulations, we have evaluated meridional shifts of the STF, Ekman transports, surface heat fluxes and Ekman pumping over the entire Southern Ocean. We focus on the data over the last 5 years of the simulation (2015-2019) relative to the CONTROL simulation to detect forcing related changes over intrinsic variability.

To test the STF response, following Figure 1, anomalies for the top 100m temperatures, surface heat fluxes, Ekman transports, Ekman pumping, mixed layer depths (MLD), potential vorticity and meridional 100m temperature gradient have been computed over a latitudinal range of ±2.5° latitude over the mean STF location (2004-2019, hereafter $STF_{CONTROL}$). MLDs have been identified as depths where the potential density difference exceeds 0.01 kg/m^3 compared to the surface layer. Potential vorticity has been calculated using the local Coriolis parameter divided by the local water depth. Chl-a anomalies have been computed for a 5° latitude band south of the mean STF location. In addition, we have zonally averaged all data sources in 5° longitude bands.

3. Results and discussion

3.1. Wind sensitivity simulations

Both SHIFT and INCREASE simulations show changes in the location of the STF of ±2° in latitude over the last 5 years (2015-2019) in comparison to CONTROL (Figure 2a-b). In INCREASE (blue lines) the displacement of the STF is predominantly northward, in agreement with Figure 1. In SHIFT, the STF migrates predominantly southward, but considerably less than expected compared to the applied 2° degree shifted winds by the end of 2019. In both sensitivity simulations the STF response is not-uniform with longitude (Figure 2b). Furthermore, the magnitude of meridional displacement in either INCREASE or SHIFT simulations is not linked to changes in ocean bathymetry (black line here represented by potential vorticity). This differentiates the surface intensified STF from other fronts in the Southern Ocean, which are directly influenced by bottom topography due to their barotropic nature (Thompson and Sallée 2012). The regions where the sign of the STF anomaly aligns with the sign of the Ekman anomaly (Figure 1) are represented by the horizontal bars at the top of Figure 2b. In SHIFT the STF response follows the proposed Ekman transport (red horizontal bar in Figure 2b) over parts of the Agulhas region, the central Indian Ocean, south of Australia to 160°E, over small parts of the central Pacific Ocean (~130°W), the eastern Pacific Ocean and east of the Malvinas Current. In INCREASE, similar regions to SHIFT show an agreement between the STF response and the Ekman transport (blue horizontal bar), but not for the western boundary currents. The different behavior for the boundary currents can explained by the Sverdrup balance, with an increase in basin-wide wind stress curl in INCREASE (Figure S4c). That leads to an increase in the strength of the western boundary currents, which shifts the STF southward in these regions, against the local enhanced northward Ekman forcing (Figure S2c). In SHIFT the impact on western boundary currents and open ocean is the same and both tend to shift south.

The surface heat flux anomalies (Figure 2c) over the $STF_{CONTROL}$ co-vary in most regions with the sign and magnitude of the STF displacement from Figure 2b in SHIFT (red horizontal bar). In INCREASE, exceptions occur in regions of high mesoscale activity, illustrated by sea surface height variance (black line in Figure 2c). Regions of high mesoscale activity are between 60°-70°E, part of the Agulhas Return Current, around 100°E where a branch of the Super Gyre crosses the STF, around 150°E where the East Australian Current Extension overshoots, around 180° where the STF detaches from the Chatham Rise, around 110°W in middle of the Pacific Ocean and at 30°W within the Malvinas Current. These regions of alignment with Figure 1 overlap with regions identified in Figure 2b.

The sign of the induced Ekman transport anomalies aligns with Figure 1 (horizontal bars in Figure 2d and see Figure S2), while the magnitude varies zonally due to the actual strength of the zonal winds and the pathway of the STF. The magnitude of the Ekman transport anomalies does not correlate with the magnitude of meridional STF shift, locally. Nevertheless, the overall Ekman transport anomaly in INCREASE is larger in comparison to SHIFT and consequently a larger STF displacement is seen in INCREASE compared to SHIFT. Furthermore, the largest Ekman transport anomalies are located over the Indian Ocean in INCREASE and SHIFT, which is also the ocean basin showing the largest meridional STF shift. In addition, this is also the region with the deepest MLDs for the STF of about 130m (black curve). MLDs of about 100m or deeper would allow that surface heat flux anomalies and heat advection to directly influence the location of the STF, while shallower MLDs would prevent this direct impact. MLDs over the central Pacific and eastern Pacific Ocean are only 60m deep, which may explain the smaller STF changes in the Pacific Ocean. This would suggest that surface heat fluxes and heat advection alone cannot penetrate deep enough to impact the STF directly, and potentially limit the STF response in these regions.

The Ekman pumping response aligns with Figure 1 for INCREASE for most longitudes, but less so for SHIFT (Figure 2e, see also Figures S4-S5). Reasons for the discrepancy in SHIFT might be due to an overall smaller applied perturbation in SHIFT, compared to INCREASE, which might not be large enough to overcome the intrinsic variability. The meridional temperature gradient (black line) is elevated in regions with higher mesoscale variability and restricts the meridional shift of the STF. A smaller meridional temperature gradient would allow for a larger meridional displacement of the STF with the same perturbation.

Overall, these sensitivity tests suggest a link between STF displacement and local Ekman transport in regions away from energetic western boundary currents. While the direction of displacement follows the sign of the Ekman transport anomalies, the local magnitude of STF displacement cannot be directly attributed to the magnitude of Ekman transport anomaly. Here, the local oceanographic conditions, such as horizontal temperature gradient and presence of oceanic currents also impact the magnitude of the displacement. The applied wind anomalies are stronger than the observed natural trends and therefore the initiated response might be stronger than in the real world. Nevertheless, the actual modelled STF response to these wind anomalies was weaker than expected due to the dampening effect of the thermal restoring, by prescribing the same SSTs across all simulations. We have defined the STF by the 11°C isotherm at 100m depths (Orsi et al., 1995), which reduces the impact of the thermal restoring. However future studies could use fully coupled models to evaluate the STF response to these wind changes to eliminate this shortcoming.

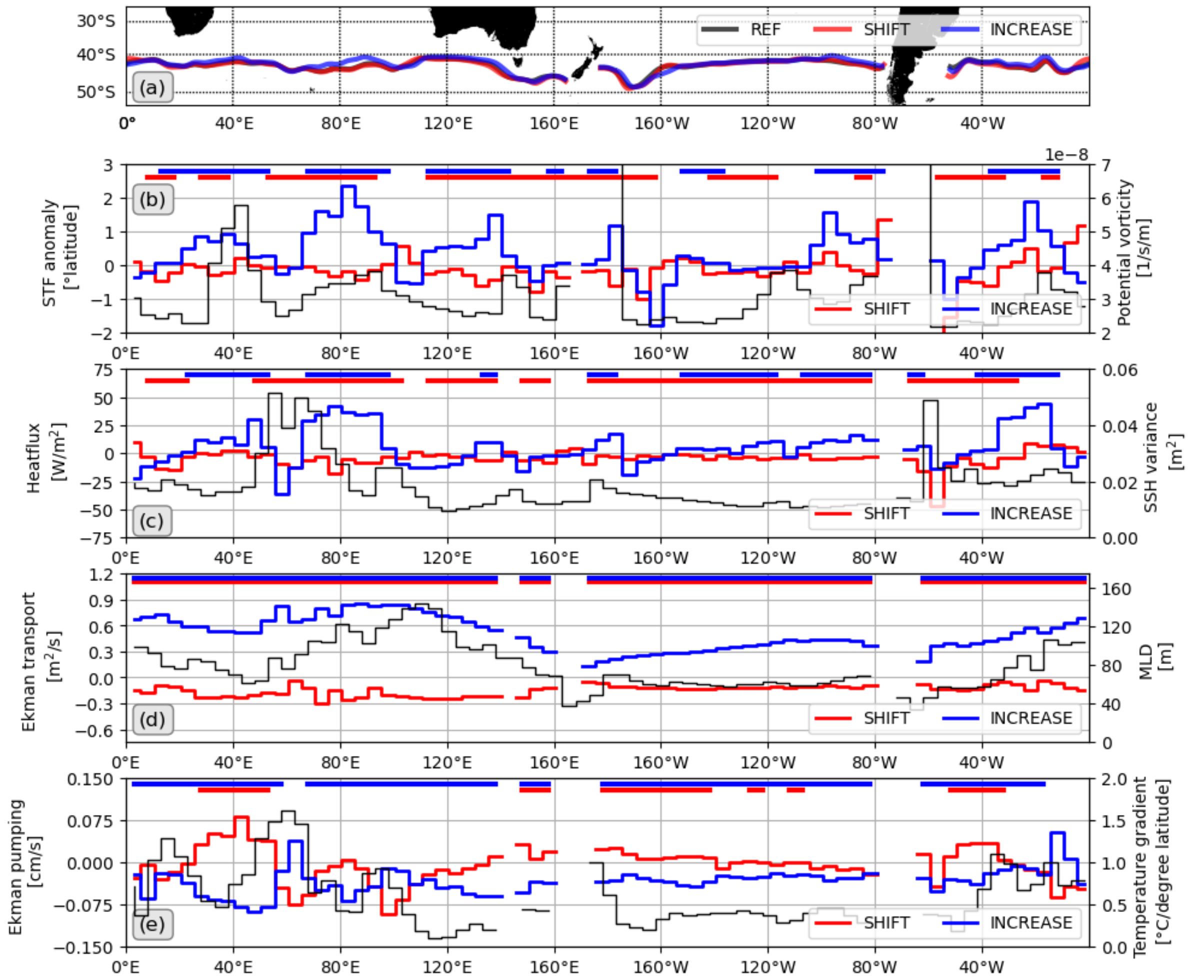

Figure 2: 2015-2019 anomalies for INCREASE and SHIFT relative to CONTROL: (a) STF location, (b) STF location anomaly and potential vorticity (f/h) from CONTROL, (c) surface heat flux anomaly and mean sea surface height (SSH) variance from CONTROL, (d) Ekman transport anomaly and mean mixed layer depth (MLD) from CONTROL, (e) Ekman pumping anomaly and meridional 100m temperature gradient from CONTROL. The anomalies are computed over the mean path (±2.5° latitude) of the $STF_{CONTROL}$. The straight coloured bars at the top indicate where the sign of anomalies align with the Figure 1 schematic. Results in (b)-(e) have been binned to 5° longitude bins.

3.2. Drivers of interannual observed variability of the STF

In this section we test if and where this above-described physical conceptual model can be applied to understand the observed interannual variability of the STF between 2004-2019 using temperature from Argo floats (Argo data only available from 2004 onwards), and the biological response through satellite observed Chl-a anomalies. In doing so we aim to identify regions where Ekman transport can explain past STF variability, and regions where other drivers are at play.

The observed top 100m temperature anomalies from Argo show interannual variations in the order of ± 0.8°C and an overall positive trend over the period 2004 to 2019 (Figure 2a and see section 3.3). The modelled top 100m temperature anomalies align with the observed anomalies (Figure 2b) in time, space and magnitude for most regions. This good match suggests a good performance of NZ20 to simulate past STF variability. The exception is large fluctuations on spatial and interannual scales between 0 and 60°E, which is the region impacted by the Agulhas Retroflection and Return Current.

In particular, the larger modelled temperature anomalies (<-0.5°C, >0.5°C) co-align with the sign of the model Ekman transport anomalies (non-hatched anomalies in Figure 2b and 2c) as expected from Figure 1. In addition, the magnitude of the Ekman transport anomalies appears to be reflected in the magnitude of the temperature anomalies. The top 100m temperature anomalies consequently generate a very similar pattern in the meridional displacement of the STF (Figure 2d-e) in Argo and in the model. The modelled surface heat fluxes over the STF (Figure 3f) exhibit more variability in space and time than the Ekman transports (Figure 3c). This suggests that the observed heat fluxes are not entirely driven by Ekman transports alone as they are in both sensitivity simulations SHIFT and INCREASE. In the real-world wind changes also influence surface air temperature anomalies via advection and impact heat flux anomalies. Despite the larger variability, the sign of surface heat flux anomalies and modelled STF displacement aligns with what is expected in Figure 1 in many regions, as shown in Figure 3e,f by the non-hatched anomalies.

Now we assess the biological response in relation to shifts of the STF, by analyzing Chl-a anomalies up to 5° south of the mean location of the STF (Figure 2g). For most longitudes there is a positive Chl-a trend, which corresponds to the positive temperature trend (Figure 2a and section 3.3) and an overall southward shift of the STF (Figure 2d) between 2004-2019. The sign of Chl-a and STF anomalies on shorter, interannual timescales aligns in many cases with the concept in Figure 1 (non-hatched anomalies in Figure 2d,g). This is particularly true for strong (<-0.5 or >0.5 mg/m^3) Chl-a anomalies.

To assess the overall robustness of the concept in Figure 1 a simple counting of anomalies which follow the concepts in Figure 1 has been performed over the Southern Ocean for the observed and modelled data between 2004 and 2019 (Figure 2g). The small sample size (16 annual values from 2004 to 2019) restricted more sophisticated methods to be deployed to measure its robustness. Neither, a Pearson nor a Spearman correlation produced significant (>95% significant level) relationships for any of the parameters. Nevertheless, the counting suggest that the concepts of Figure 1 apply between 60-80% of the time over large parts of the Southern Ocean. Regions where the physical concept follows the concept in Figure 1 (likelihood ≥ 50% for both physical criteria) are shown by the blue horizonal bar and account for about 75% of the ocean. Regions where the physical concept fails align with regions identified in Figure 2c (black line), where mesoscale eddy variability is elevated, for example at around 60°E and 120°E where the STF interacts with the Agulhas Return Current and the southern boundary of the Super Gyre, respectively. The Syper Gyre is the combination of the three subtropical gyres in the Southern Hemisphere, diagnosed by the zero line of the barotropic streamfunction, which spearates the subtropics from the Antarctic Circumpolar Current.

If we include Chl-a in the assessment criteria with the physical criteria (orange bars, likelihood ≥ 50% for all three criteria), the concept still applies to about 50% of the ocean. We acknowledge that the 50% cut-off threshold is an arbitrary choice to prove that the concept applies since an independent normal distributed process should center around 50%. Nevertheless, since these processes are biophysically linked, the probability that they randomly co-occur are unlikely. The geographical coherence of this agreement and disagreement provides further evidence that the concept applies in many regions. This concept fails in regions where the STF interacts with strong western boundary currents and subsequent elevated eddy activity.

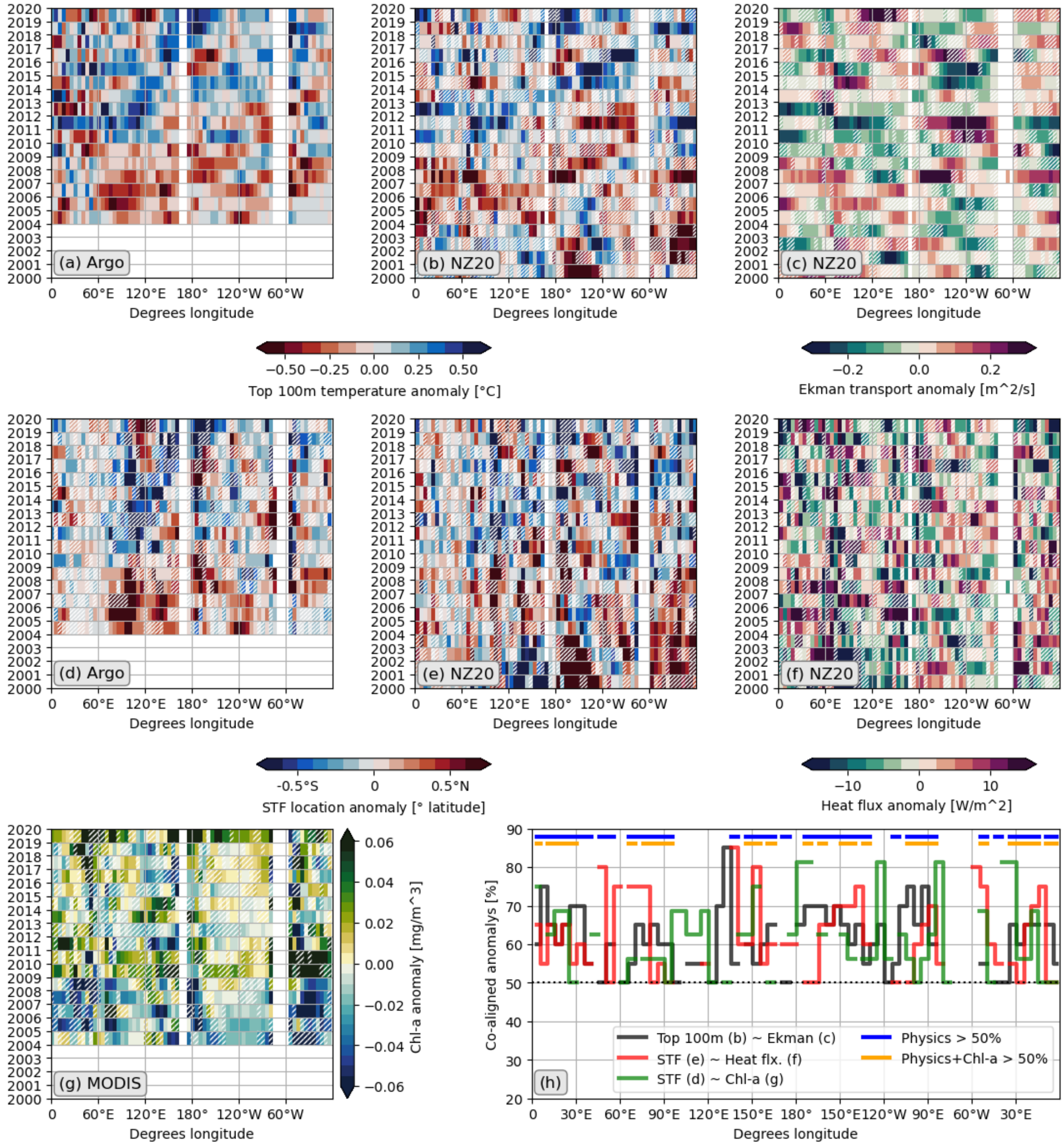

Figure 3. (a) Top 100m Argo temperature anomaly relative to the period 2004-2019 (b) Same as (a) but for NZ20. (c) NZ20 Ekman transport anomaly. Hatching in (b) and (c) indicates where the sign of top 100m temperature and Ekman transport anomalies does not align with the concept in Figure 1. (d) Argo meridional STF location anomaly in ° latitude. (e) same as (d) but for NZ20. (f) surface heat flux anomalies from NZ20 where positive anomalies indicate a heat flux into the ocean. Hatching in (e) and (f) indicates where the sign of STF location and surface heat fluxes anomalies does not align with the concept in Figure 1. (g) MODIS chlorophyll-a anomaly. Hatching in d) and (g) indicates where the sign of chlorophyll-a and Argo STF anomalies does not align with the concept in Figure 1. (h) How often anomalies align between Ekman transport versus top 100m temperature in NZ20 (black), heat flux anomalies versus STF anomalies from NZ20 (red) and Argo STF anomalies and Chl-a anomalies

(green) with the concept from Figure 1. Blue (orange) bar indicates where the black and red (and green) line shows at least an agreement of ≥ 50% over time. All anomalies (a) - (f) are extracted over the mean STF location (±2.5° latitude band, 2004-2019). Chl-a anomalies are extract between the mean Argo STF location and 5° south of it. Observations and model results have been binned to 5° longitude bins.

3.3. Observed trends in STF location from Argo SST and Chl-a between 2004 to 2019

Based on the concept outlined above, a southward shift of the westerly winds would promote a southward shift of the STF, while stronger westerly winds will increase the northward Ekman transport and initiate a northward shift of the STF (see Figure 1 and section 3.1). The consequence of these factors combined could be that the STF does not shift if both factors balance each other.

The Argo STF trends are mostly small (<0.25° latitude per decade, black line in Figure 4a), but show a predominantly southward directed trend following the southward shifted westerly winds. Larger southwards trends (>0.5° latitude per decade) are seen between 70°E to 105°E, 130°E-160°W and between 180 and 160°E. The southward shift of the STF goes along with positive Chl-a trends south of the mean location of the Argo STF (green line), as expected with the concept proposed in Figure 1 (red bar in Figure 4a). Nevertheless, the actual Argo STF trends are smaller than the expected STF trend, based on the changes in the position of the zero wind stress curl (Qu et al. 2018) and the location of the maximum westerly winds (Figure S1d), which both show a southward trend of ~0.4° latitude/decade. We argue that this mis-match, between expected and actual STF trends, is related to changes in local winds (i.e. zonal wind, blue line) and the consequential Ekman forcing. In regions where the zonal wind trend is positive over the STF, the observed STF trend is smaller than the expected STF trend (-0.4° latitude/decade) and conversely for negative zonal wind trends. Regions which follow this concept are shown by the purple bar in Figure 4a and align with regions of alignment identified in the previous sections. Exceptions from the concept again match with regions of elevated eddy variability, where the STF encounters currents.

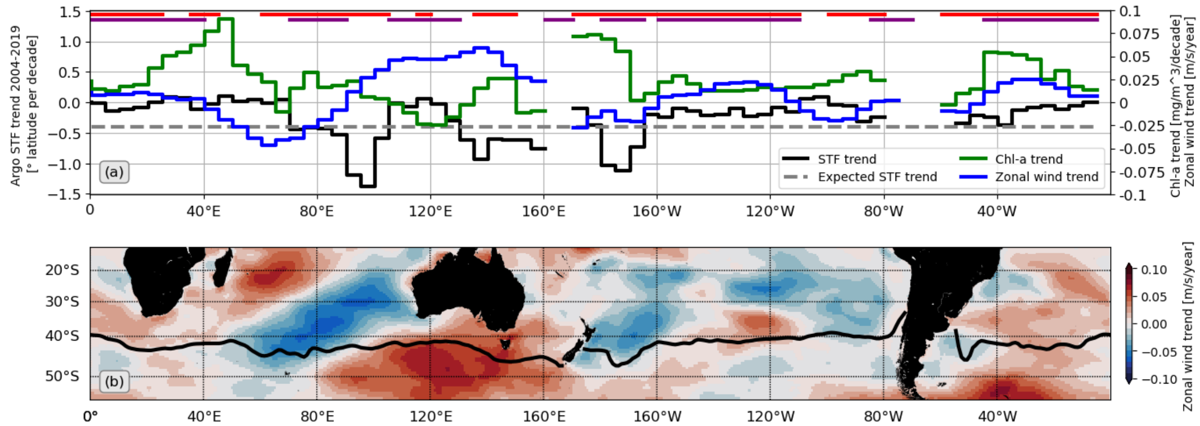

Figure 4. (a) Trends in the meridional location of the STF based on Argo SST data from 2004-2019 (black line) and trends in Chl-a concentrations (green line). Zonal wind trends are extracted over the mean location of the STF (±2.5° latitude band, 2004-2019), while the Chl-a trends are the average Chl-a anomaly over a 5° latitude band south of the mean STF location. The red bar at the top indicates regions where the STF trend and Chl-a trend have the opposite sign. The purple bar indicates regions where zonal wind trends can explain the observed STF trend in relation to the expected STF trend (-0.4° latitude/decade, indicate by the grey dashed line). (b) Zonal wind trend from JRA-55-DO from 2004-2019 is shown by the color shading and Argo mean STF location by the black line. The blue line in 4a is based on this trend over the STF.

The observed southward trend of the STF goes in hand with a poleward habitat expansion of subtropical species (Law et al. 2017; Shears and Bowen 2017) and is related to the observed poleward expansion of the subtropical gyres (Yang et al. 2020). In this context accelerated warming over the western boundary currents has been observed (Wu et al. 2012) and had cascading effects on the marine ecosystems via marine heatwaves (Smale et al. 2019). Our results together with others (e.g. Del Castillo et al. (2019), Carranza and Gille (2015); Montie et al. (2020)) suggest an increase in biological productivity in the Southern Ocean over the past decades, based on increasing Chl-a concentrations and a positive link to temperature. This increase has implications for the foodweb, and the fisheries of the STF. However, how these Chl-a trends will impact fish, fisheries, and the biological carbon pump is complex and not well understood. Nevertheless, future climate projections suggest that southernmost western boundary currents will further intensify (Qu et al. 2019; Sen Gupta et al. 2021), subtropical gyres will continue to expand poleward (Yang et al. 2020) and marine heatwaves will become more intense and frequent and impact the STF (Behrens et al. 2022; Oliver et al. 2019). More research is needed to robustly quantify the impacts of these physical changes on the biology and the ecosystems associated with the STF.

4. Conclusions

This paper explores how changes in surface winds can alter the location of the STF. We have tested how a southerly shift, or an increase of the westerly winds over the Southern Ocean can impact the meridional location of the STF. We tested if and where Ekman dynamics can be applied to explain the meridional shift in the STF and in which regions other drivers control the response.

In two sensitivity simulations a trend pattern to surface winds was applied over a 20-year period to investigate the transient response to these wind anomalies. The results from the sensitivity simulations and analyses of the past observed STF variability over the last 20 years have demonstrated that STF shifts, away from ocean currents, can be explained in the first-instance by changes in the Ekman transports as a consequence of the zonal wind stress anomalies over the STF (±2.5° longitude). Stronger westerly winds increase the northward Ekman transport and cause the STF to shift northward. Southward shifted winds, which results in locally reduced westerly winds reduces the Ekman transport and the STF shifts southward. However, the actual magnitude of the meridional displacement depends strongly on the local conditions (e.g., oceanic currents, stratification, and meridional temperature gradient). Nevertheless, regions where Ekman transport anomalies are largest tend to show the larger meridional displacements. The STF does not follow the Ekman response in regions where it interacts with ocean boundary currents. In these boundary current regions the STF is dominated by the Sverdrup balance and increases in westerly winds push the STF southward despite positive Ekman anomalies, as the strength of the boundary currents increases and offsets the Ekman forces. Other exceptions are regions where mesoscale eddy activity is high. In these regions the STF does not show robust links with Ekman transport anomalies.

Over the period 2004-2019 the observed southward trend of the STF is less than the expected southward trend in most regions, based on the overall southward shift of the zero wind stress curl and maximum in zonal winds, which both show a southward trend of 0.4° latitude per decade. We argue that the discrepancy between expected and actual shift of the STF can be explained by trends in the Ekman forcing, which are asymmetric and oppose the southward trend caused by the shift in some regions. The regions where local Ekman transports cannot explain the actual shift of the STF are very consistent between interannual and decade timescales and align with regions of mesoscale variability and strong oceanic currents such as in the vicinity of western boundary currents.

Changes in the location of the STF have profound implications on Chl-a concentrations, which provides motivation to improve our understanding about the physical driver of these STF shifts. A southward shifted STF generates negative Chl-a anomalies north of its previous STF position and negative Chl-a anomalies to its north, with implications on the local ecosystem and carbon fluxes. While the sign of the Chl-a anomalies follows the direction of the STF shift, the magnitude of the Chl-a anomalies does not necessarily correspond to the magnitude of the STF shift. Here, the local conditions (e.g., nutrient concentrations) are important. Nevertheless, the impact on boundary current transports and Chl-a might be more nuanced due to the asymmetry of wind trends over the Southern Ocean (Beal and Elipot 2016; Goyal et al. 2021; Noh et al. 2021; Sallée et al. 2010; Waugh et al. 2020), which results in regional variations. Here more regional studies are needed to understand the local response.

5. Acknowledgements

This paper obtained funding and support through the Royal Society Marsden Fund (NIW1701) and funding from the Ministry of Business, Innovation and Employment through the Deep South National Science Challenge (C01X1902). We would like to acknowledge the collaboration with MetOffice (UK) and the NeSI High Performance Computing Facility team for their technical support. Finally, I would like to acknowledge my partner, son, and daughter. Data used for this study can be freely accessed through: https://doi.org/10.5281/zenodo.6837010 .

6. References

Barnier, B., and Coauthors, 2006: Impact of partial steps and momentum advection schemes in a global ocean circulation model at eddy-permitting resolution. *Ocean Dynam*, **56,** 543-567.

Beal, L. M., and S. Elipot, 2016: Broadening not strengthening of the Agulhas Current since the early 1990s. *Nature*, **540,** 570-+.

Behrens, E., A. M. Hogg, M. H. England, and H. Bostock, 2021: Seasonal and Interannual Variability of the Subtropical Front in the New Zealand Region. *Journal of Geophysical Research: Oceans*, **126,** e2020JC016412.

Behrens, E., G. Rickard, O. Morgenstern, T. Martin, A. Osprey, and M. Joshi, 2016: Southern Ocean deep convection in global climate models: A driver for variability of subpolar gyres and Drake Passage transport on decadal timescales. *Journal of Geophysical Research: Oceans*, **121,** 3905--3925.

Behrens, E., G. Rickard, S. Rosier, J. Williams, O. Morgenstern, and D. Stone, 2022: Projections of Future Marine Heatwaves for the Oceans Around New Zealand Using New Zealand's Earth System Model. *Frontiers in Climate*, **4**.

Belkin, I. M., 2021: Subtropical Frontal Zone of the Southern Ocean.

Belkin, I. M., and A. L. Gordon, 1996: Southern Ocean fronts from the Greenwich meridian to Tasmania. *J Geophys Res-Oceans*, **101,** 3675-3696.

Carranza, M. M., and S. T. Gille, 2015: Southern Ocean wind-driven entrainment enhances satellite chlorophyll-a through the summer. *Journal of Geophysical Research: Oceans*, **120,** 304-323.

Chapman, C. C., M.-A. Lea, A. Meyer, J.-B. Sallée, and M. Hindell, 2020: Defining Southern Ocean fronts and their influence on biological and physical processes in a changing climate. *Nature Climate Change*, **10,** 209-219.

Chiswell, S. M., J. Bradford-Grieve, M. G. Hadfield, and S. C. Kennan, 2013: Climatology of surface chlorophylla, autumn-winter and spring blooms in the southwest Pacific Ocean. *Journal of Geophysical Research: Oceans*, **118,** 1003-1018.

De Boer, A. M., R. M. Graham, M. D. Thomas, and K. E. Kohfeld, 2013: The control of the Southern Hemisphere Westerlies on the position of the Subtropical Front. *Journal of Geophysical Research: Oceans*, **118,** 5669-5675.

Deacon, G. E. R., 1982: Physical and Biological Zonation in the Southern-Ocean. *Deep-Sea Res*, **29,** 1-15.

Debreu, L., C. Vouland, and E. Blayo, 2008: AGRIF: Adaptive grid refinement in Fortran. *Computers & Geosciences*, **34,** 8-13.

Del Castillo, C. E., S. R. Signorini, E. M. Karaköylü, and S. Rivero-Calle, 2019: Is the Southern Ocean Getting Greener? *Geophysical Research Letters*, **46,** 6034-6040.

Frankcombe, L. M., P. Spence, A. M. Hogg, M. H. England, and S. M. Griffies, 2013: Sea level changes forced by Southern Ocean winds. *Geophysical Research Letters*, **40,** 5710-5715.

Good, S. A., M. J. Martin, and N. A. Rayner, 2013: EN4: Quality controlled ocean temperature and salinity profiles and monthly objective analyses with uncertainty estimates. *Journal of Geophysical Research: Oceans*, **118,** 6704--6716.

Goyal, R., M. H. England, M. Jucker, and A. Sen Gupta, 2021: Response of Southern Hemisphere Western Boundary Current Regions to Future Zonally Symmetric and Asymmetric Atmospheric Changes. *Journal of Geophysical Research: Oceans*, **126**.

Graham, R. M., A. M. de Boer, K. J. Heywood, M. R. Chapman, and D. P. Stevens, 2012: Southern Ocean fronts: Controlled by wind or topography? *J Geophys Res-Oceans*, **117,** C08018.

Hunke, E. C., and W. H. Lipscomb, 2010: CICE: The Los Alamos Sea Ice Model, Documentation and Software User's Manual, Version 4.1.

Law, C. S., G. J. Rickard, S. E. Mikaloff-Fletcher, M. H. Pinkerton, E. Behrens, S. M. Chiswell, and K. Currie, 2017: Climate change projections for the surface ocean around New Zealand. *New Zeal J Mar Fresh***,** 1--27.

Lenn, Y.-D., and T. K. Chereskin, 2009: Observations of Ekman currents in the Southern Ocean. *J Phys Oceanogr*, **39,** 768-779.

Lovenduski, N. S., 2005: Impact of the Southern Annular Mode on Southern Ocean circulation and biology. *Geophysical Research Letters*, **32,** L11603.

Madec, G., and Coauthors, 2017: NEMO ocean engine.

Montie, S., M. S. Thomsen, W. Rack, and P. A. Broady, 2020: Extreme summer marine heatwaves increase chlorophyll a in the Southern Ocean. *Antarctic Science*, **32,** 508-509.

Noh, K. M., H.-G. Lim, and J.-S. Kug, 2021: Zonally asymmetric phytoplankton response to the Southern annular mode in the marginal sea of the Southern ocean. *Scientific Reports*, **11,** 10266.

Oliver, E. C. J., and Coauthors, 2019: Projected Marine Heatwaves in the 21st Century and the Potential for Ecological Impact. *Frontiers in Marine Science*, **6**.

Orsi, A. H., T. Whitworth, and W. D. Nowlin, 1995: On the Meridional Extent and Fronts of the Antarctic Circumpolar Current. *Deep-Sea Res Pt I*, **42,** 641-673.

Pinkerton, M., K. Richardson, P. Boyd, M. Gall, J. Zeldis, M. Oliver, and R. Murphy, 2005: Intercomparison of ocean colour band-ratio algorithms for chlorophyll concentration in the Subtropical Front east of New Zealand. *Remote Sens Environ*, **97,** 382-402.

Qu, T., I. Fukumori, and R. A. Fine, 2018: Spin-up of the Southern Hemisphere Super Gyre. *Journal of Geophysical Research: Oceans*, **124,** 2018JC014391.

Qu, T. D., I. Fukumori, and R. A. Fine, 2019: Spin-Up of the Southern Hemisphere Super Gyre. *J Geophys Res-Oceans*, **124,** 154-170.

Roemmich, D., and J. Gilson, 2009: The 2004–2008 mean and annual cycle of temperature, salinity, and steric height in the global ocean from the Argo Program. *Progress in Oceanography*, **82,** 81--100.

Sallée, J. B., K. G. Speer, and S. R. Rintoul, 2010: Zonally asymmetric response of the Southern Ocean mixed-layer depth to the Southern Annular Mode. *Nature Geoscience*, **3,** 273-279.

Sathyendranath, S., and Coauthors, 2019: An Ocean-Colour Time Series for Use in Climate Studies: The Experience of the Ocean-Colour Climate Change Initiative (OC-CCI). *Sensors-Basel*, **19**.

Sen Gupta, A., A. Stellema, G. M. Pontes, A. S. Taschetto, A. Vergés, and V. Rossi, 2021: Future changes to the upper ocean Western Boundary Currents across two generations of climate models. *Scientific Reports*, **11**.

Shears, N. T., and M. M. Bowen, 2017: Half a century of coastal temperature records reveal complex warming trends in western boundary currents. *Scientific Reports*, **7,** 14527.

Smale, D. A., and Coauthors, 2019: Marine heatwaves threaten global biodiversity and the provision of ecosystem services. *Nature Climate Change*, **9,** 306-312.
Sokolov, S., and S. R. Rintoul, 2009: Circumpolar structure and distribution of the Antarctic Circumpolar Current fronts: 1. Mean circumpolar paths. *J Geophys Res-Oceans*, **114,** C11018.
Spence, P., J. C. Fyfe, A. Montenegro, and A. J. Weaver, 2010: Southern Ocean Response to Strengthening Winds in an Eddy-Permitting Global Climate Model. *Journal of Climate*, **23,** 5332-5343.
Spence, P., S. M. Griffies, M. H. England, A. M. Hogg, O. a. Saenko, and N. C. Jourdain, 2014: Rapid subsurface warming and circulation changes of Antarctic coastal waters by poleward shifting winds. *Geophysical Research Letters*, **41,** 4601--4610.
Storkey, D., and Coauthors, 2018: UK Global Ocean GO6 and GO7: a traceable hierarchy of model resolutions. *Geoscientific Model Development*, **11,** 3187-3213.
Sullivan, C. W., K. R. Arrigo, C. R. Mcclain, J. C. Comiso, and J. Firestone, 1993: Distributions of Phytoplankton Blooms in the Southern-Ocean. *Science*, **262,** 1832-1837.
Swart, N. C., and J. C. Fyfe, 2012: Observed and simulated changes in the Southern Hemisphere surface westerly wind-stress. *Geophysical Research Letters*, **39,** n/a--n/a.
Thompson, A. F., and J.-B. Sallée, 2012: Jets and Topography: Jet Transitions and the Impact on Transport in the Antarctic Circumpolar Current. *J Phys Oceanogr*, **42,** 956-972.
Tilburg, C. E., H. E. Hurlburt, J. J. O'Brien, and J. F. Shriver, 2002: Remote topographic forcing of a baroclinic western boundary current: An explanation for the Southland Current and the pathway of the subtropical front east of New Zealand. *J Phys Oceanogr*, **32,** 3216-3232.
Tsujino, H., and Coauthors, 2018: JRA-55 based surface dataset for driving ocean–sea-ice models (JRA55-do). *Ocean Modelling*, **130,** 79-139.
Wang, W., and R. X. Huang, 2004: Wind energy input to the Ekman layer. *J Phys Oceanogr*, **34,** 1267-1275.
Waugh, D. W., A. Banerjee, J. C. Fyfe, and L. M. Polvani, 2020: Contrasting Recent Trends in Southern Hemisphere Westerlies Across Different Ocean Basins. *Geophysical Research Letters*, **47,** e2020GL088890.
Weeks, S. J., and F. A. Shillington, 1994: Interannual scales of variation of pigment concentrations from coastal zone color scanner data in the Benguela Upwelling system and the Subtropical Convergence zone south of Africa. *Journal of Geophysical Research: Oceans*, **99,** 7385-7399.
Wu, L., and Coauthors, 2012: Enhanced warming over the global subtropical western boundary currents. *Nature Climate Change*, **2,** 161--166.
Yang, H., and Coauthors, 2020: Poleward Shift of the Major Ocean Gyres Detected in a Warming Climate. *Geophysical Research Letters*, **47**.

The modelled volume transports of CONTROL over the nested region are in close agreement with observational estimates. That applies to the East Australian Current, East Auckland Current and Tasman Leakage. Transports for Malvinas and Agulhas Currents are over and underestimated by roughly 10 Sv compared to observations, respectively. In SHIFT with exception of the East Auckland Current and Tasman Leakage, all transports show a decline in comparison to CONTROL. In INCREASE all transports with exception of the Tasman Leakage increases in comparison to CONTROL. The increasing transports in INCREASE are in agreement with the Sverdrup balance and more negative wind stress curl over the subtropical gyres. The weakening in SHIFT also aligns with changes in the large-scale wind stress curl pattern, which suggest an increase (see Figure S3). It is interesting to note that in SHIFT both the East Auckland Current and Tasman Leakage show an increase, while all previous studies found a seesaw behaviour (Behrens et al. 2019; Hill et al. 2008).

	Observations	CONTROL	SHIFT	INCREASE
East Australian Current (30°S) (southward)	22.1 Sv (Mata et al. 2000)	22.5 Sv	20.1 Sv	24.2 Sv
Malvinas Current (40°S) (northward)	41 Sv (Spadone and Provost 2009)	51.1 Sv	37 Sv	50 Sv
Agulhas Current (32°S) (southward)	73 Sv - 84 (Beal and Bryden 1999), (Beal and Elipot 2016)	58 Sv	53.8 Sv	67.8 Sv
East Auckland Current (eastward)	9 Sv (Stanton and Sutton 2003)	10.6 Sv	12.9 Sv	13.3 Sv
Tasman Leakage (westward)	10 Sv (Oliver and Holbrook 2014) 8-	11.3 Sv	16.3 Sv	8.5 Sv

Table T1. Mean volume transports for the CONTROL, SHIFT and INCREASE simulation. Values are averaged over the period 2015-2019 for East Australian Current, Malvinas Current, Agulhas Current, East Auckland Current and Tasman Leakage. Sv = 1×10^6 m3/s.

Figure S1a indicates that large interannual variability in Southern Ocean wind speed is present (zonal + meridional), without a meridional coherence between years. Figure S1b and S1c show how the zonal winds intensify over the period 2000-2019. North of ~42°S zonal winds are decreasing in strength (Figure S1c), while between 56°S to 60°S they intensify the largest by about 0.6% per year. Figure S1d shows that the maximum of the westerly winds shifts southward by 0.4° latitude per decade over the period 2000-2019.

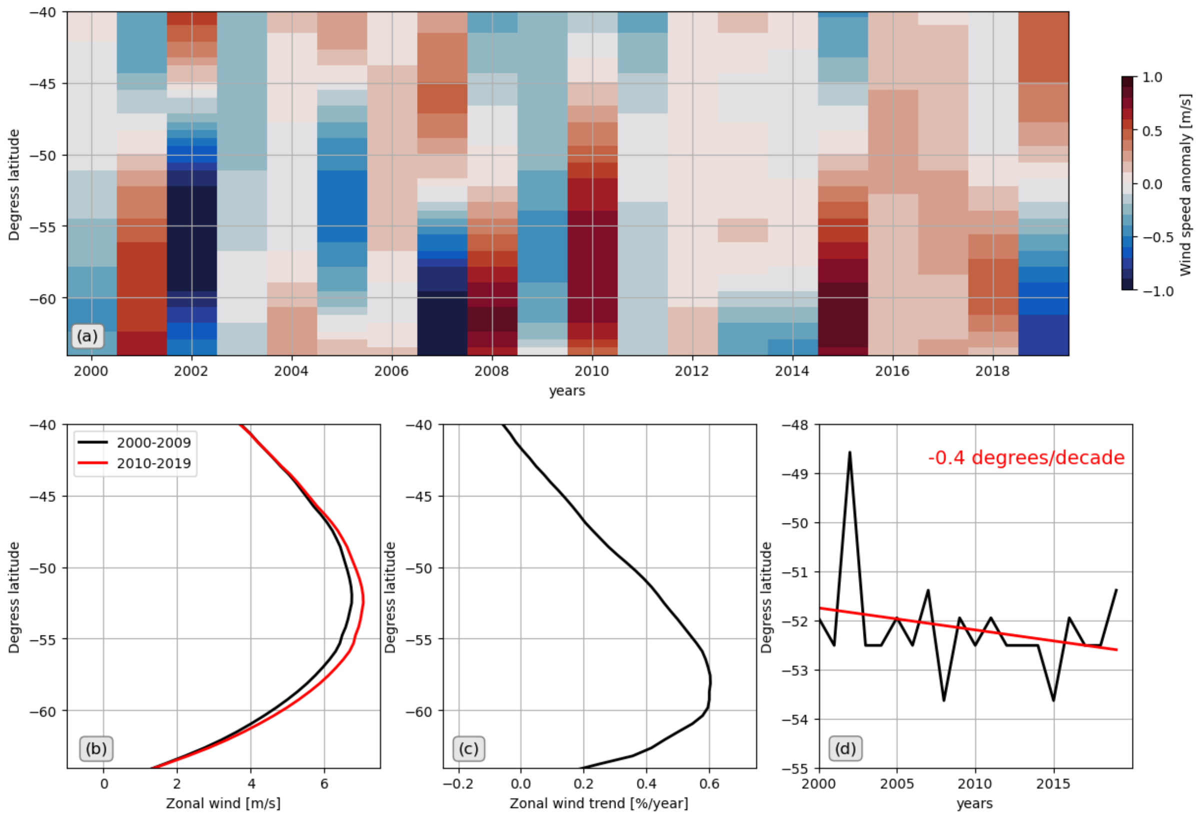

Figure S1. (a) Annual anomalies of zonally averaged (zonal + meridional) wind speeds in JRA55-DO relative to 2000-2019. (b) Zonal averaged zonal winds for the periods 2000-2009 (black) and 2010-2019 (red). (c) Percentage change per year between both periods in (b). (d) Location of maximum zonal winds (black) and linear trend (red). Red label provides the trend figure.

Figure S2a shows the northward Ekman transport over the Southern Ocean in CONTROL, which varies zonally and meridionally. Largest Ekman transports are found south of the STF. In SHIFT (Figure S2b) Ekman transports decrease, shown by the negative anomalies, over the STF. In INCREASE (Figure 2c) Ekman transports increase, shown by the positive anomalies, over the STF. Anomalies over the STF in INCREASE are largen than in SHIFT. (see also Figure 1)

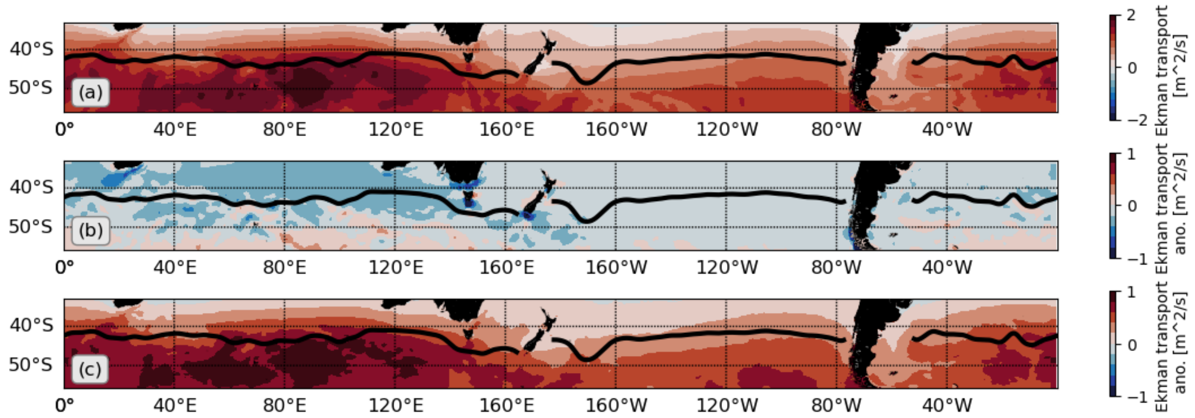

Figure S2. Ekman transport and anomalies averaged over the period 2015-2019. (a) CONTROL, (b) SHIFT-CONTROL, (c) INCREASE-CONTROL. The black line shows the mean location of the STF from CONTROL. Positive Ekman transports reflect a northward transport.

Figure S3a shows that heat fluxes over the western boundary currents (negative fluxes) and their extensions are directed from the ocean to the atmosphere in CONTROL. South of the STF heat fluxes are directed predominantly from the atmosphere into the ocean (positive fluxes). In SHIFT (Figure S3b) heat flux anomalies over the STF are mainly negative, which indicates a heat flux towards the atmosphere as this region warms. In INCREASE (Figure S3c) the response is more variable than in SHIFT over the STF. Over the boundary currents heat flux anomalies are negative as they intensify. Away from these currents heat fluxes are predominantly negative due to increased northward Ekman transports of cold water (Figure S2c). (see also Figure 1)

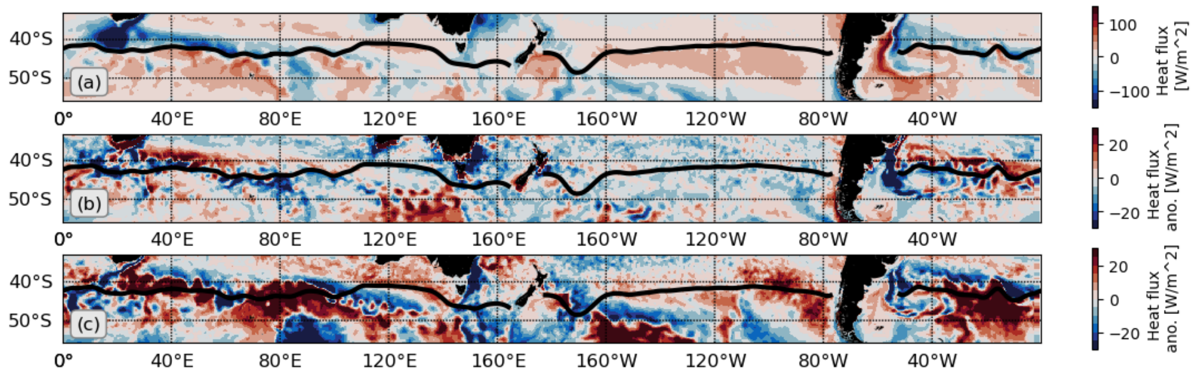

Figure S3. Surface heat flux and anomalies averaged over the period 2015-2019. (a) CONTROL, (b) SHIFT-CONTROL, (c) INCREASE-CONTROL. The black line shows the mean location of the STF from CONTROL. Positive surface heat fluxes indicate fluxes from the atmosphere into the ocean.

Figure S4a shows Ekman downwelling (negative values) over the subtropical regions and over the STF. In SHIFT (Figure S4b) Ekman pumping anomalies over the STF are mainly positive, which indicates less downwelling as the STF shifts south. In INCREASE (Figure S4c) Ekman pumping anomalies over the STF are mainly negative, which suggest more downwelling. (see also Figure 1)

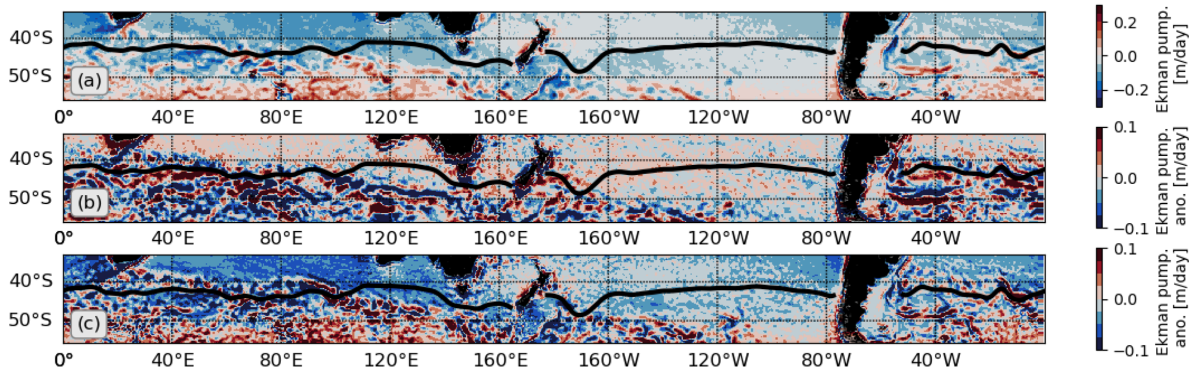

Figure S4. Ekman pumping and anomalies averaged over the period 2015-2019. (a) CONTROL, (b) SHIFT-CONTROL, (c) INCREASE-CONTROL. The black line shows the mean location of the STF from CONTROL. Negative Ekman pumping indicates a downward motion.

The temperature anomalies in SHIFT (Figure S5b) are positive over most parts of water column due to decreased Ekman transports. The location of the STF does not vary for this particular longitude. In INCREASE (Figure S5c) negative temperature anomalies are present over the upper water column due to increased Ekman transports. In INCREASE the STF shift northward over this longitude band.

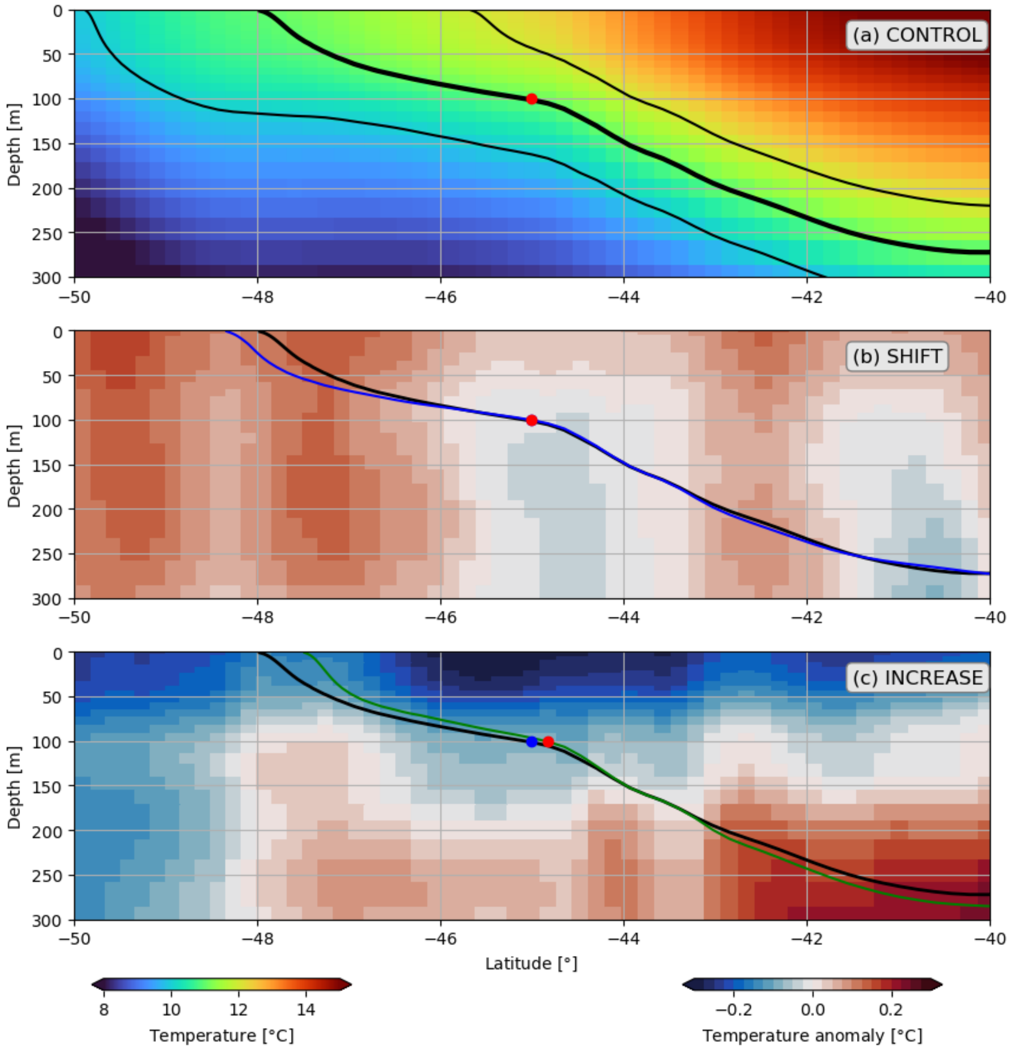

Figure S5. Temperature section and anomalies averaged between 180° to 160°W over the period 2015-2019. (a) CONTROL, (b) SHIFT-CONTROL and (c) INCREASE—CONTROL. Black contour lines in (a) mark the 10°C, 11°C (bold) and 12°C isotherm. The red dot marks the location of the STF (11°C isotherm at 100m depth). The blue and green lines in (b) and (c) mark the 11°C isotherm in SHIFT and INCREASE in relation to CONTROL (black line). The blue dots in (b,c) is the location of the STF from CONTROL, and the red dots represent the actual STF location in SHIFT and INCREASE, respectively.

Negative correlations over large parts of the STF in Figure S6a indicate that increased Ekman transports are associated with a decline in the top 100m temperatures. That is also reflected by the positive correlations in Figure S6b over the STF, which indicates that a northward shift of the STF, due a decline in temperatures causes additional heat fluxes from the atmosphere into the ocean.

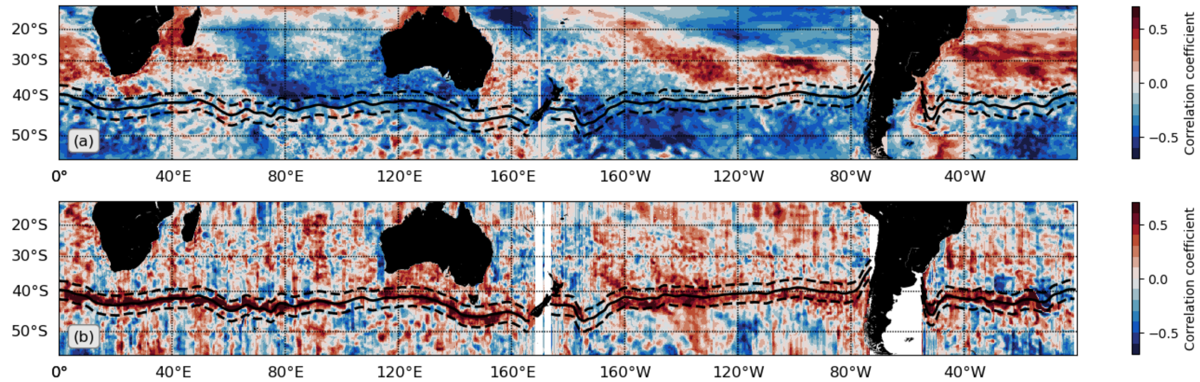

Figure S6. Pearson correlation coefficient between annual anomalies from NZ20 of (a) Ekman transport over the STF (±2.5° latitude) and top 100m averaged temperature, (b) meridional shifts of the STF and heat flux. The solid black line shows the mean location of STF from NZ20 for the period 2004-2019 and the dashed lines the ±2.5° latitude band over which the anomalies have been averaged for Figure 3b-c, 3e-f and 3h. Positive surface heat fluxes represent a heat flux from the atmosphere into the ocean.

The positive correlations south of the STF over large parts of the Southern Ocean in Figure S7a indicate that Chl-a concentration increase if top 100m temperatures increase in these regions, while they are negatively correlated north of the STF. This relation can then be linked to shifts in the STF (Figure S7b) where a southward shift of the STF is associated with a decline in Chl-a concentrations, south of the STF.

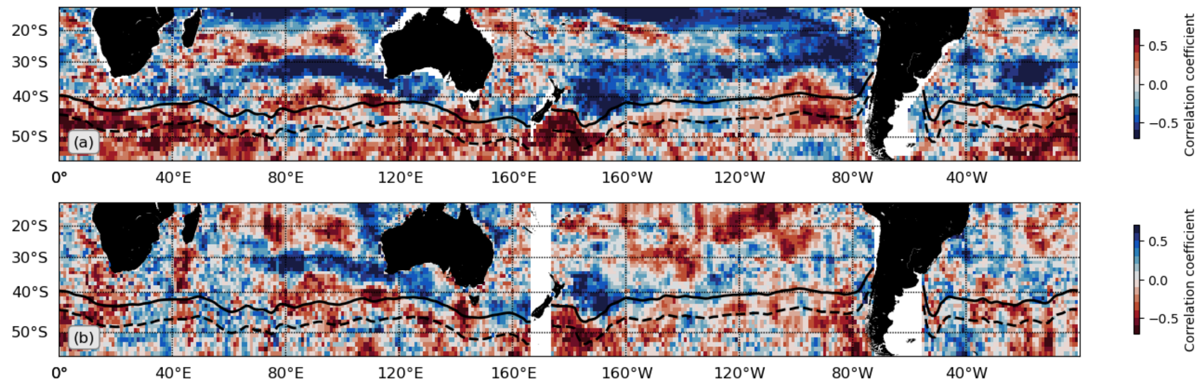

Figure S7. Pearson correlation coefficient between annual anomalies from Argo of (a) Chl-a and top 100m averaged temperature anomaly, (b) Chl-a and meridional shifts of the STF. The solid black line shows the mean location of STF from Argo for the period 2004-2019 and the dashed line the 5° southern boundary over which the anomalies have been averaged for Figure 3g and 3h. Note in (b) the colour scale has been inverted.

References:

Beal, L. M., and H. L. Bryden, 1999: The velocity and vorticity structure of the Agulhas Current at 32°S. *Journal of Geophysical Research: Oceans*, **104,** 5151-5176.

Beal, L. M., and S. Elipot, 2016: Broadening not strengthening of the Agulhas Current since the early 1990s. *Nature*, **540,** 570-573.

Behrens, E., D. Fernandez, and P. Sutton, 2019: Meridional oceanic heat transport influences marine heatwaves in the Tasman Sea on interannual to decadal timescales. *Frontiers in Marine Science*, **6,** 228.

Hill, K. L., S. R. Rintoul, R. Coleman, and K. R. Ridgway, 2008: Wind forced low frequency variability of the East Australia Current. *Geophysical Research Letters*, **35,** L08602.

Mata, M. M., M. Tomczak, S. Wijffels, and J. A. Church, 2000: East Australian Current volume transports at 30°S: Estimates from the World Ocean Circulation Experiment hydrographic sections PR11/P6 and the PCM3 current meter array. *Journal of Geophysical Research: Oceans*, **105,** 28509--28526.

Oliver, E. C. J., and N. J. Holbrook, 2014: Extending our understanding of South Pacific gyre spin-up : Modeling the East Australian Current in a future climate. *Journal of Geophysical Research: Oceans*, **119,** 2788--2805.

Spadone, A., and C. Provost, 2009: Variations in the Malvinas Current volume transport since October 1992. *Journal of Geophysical Research: Oceans*, **114**.

Stanton, B., and P. Sutton, 2003: Velocity measurements in the East Auckland Current north-east of North Cape, New Zealand. *New Zeal J Mar Fresh*, **37,** 195--204.